



Large-Eddy Simulations of Reactive Pollutant Dispersion in the Convective Boundary Layer over Flat and Urban-Like Surfaces

Beom-Soon Han¹ · Jong-Jin Baik¹ · Seung-Bu Park² · Kyung-Hwan Kwak³

Received: 12 July 2018 / Accepted: 21 March 2019 / Published online: 4 April 2019
© Springer Nature B.V. 2019

Abstract

Turbulent flow and reactive pollutant dispersion in the convective boundary layer (CBL) over flat and urban-like surfaces are investigated using a large-eddy simulation model with NO–NO₂–O₃ chemistry, with the urban-like surface represented by a block array. The CBL over a flat surface with and without ambient flow (FW and FNW cases, respectively) and the CBL over a block array with and without ambient flow (BW and BNW cases, respectively) are simulated. Wind shear in the entrainment zone increases the turbulence intensity and enhances the heat exchange in the entrainment zone. The urban-like surface induces greater wind shear in the entrainment zone, thus the largest turbulence intensity and heat exchange are found in the BW case. High NO concentration appears in updraft regions, whereas high O₃ concentration appears in downdraft regions. The segregation of NO and O₃ reduces the O₃ decomposition in the CBL. The magnitude of the vertical gradients of NO, NO₂, and O₃ concentrations in the entrainment zone is smallest in the BW case, indicating that the largest reactive pollutant exchange occurs in the BW case. It seems that the greater wind shear in the entrainment zone induced by the urban-like surface also enhances the reactive pollutant exchange in the entrainment zone. The magnitude of the O₃ production rate in the entrainment zone is large due to the mixing of mixed-layer air with air in the entrainment zone, especially around updraft regions. Since the segregation of NO and O₃ interrupts the O₃ decomposition, the turbulent component of the O₃ production rate is generally positive in the CBL. The reduction of the O₃ decomposition due to the segregation in the entrainment zone is smallest in the BW case. The effects of segregation on the chemical reactions are reduced due to the strengthened turbulent motions in the BW case.

Keywords Convective boundary layer · Entrainment zone · Large-eddy simulation · Reactive pollutant dispersion · Urban-like surface

✉ Jong-Jin Baik
jjbaik@snu.ac.kr

¹ School of Earth and Environmental Sciences, Seoul National University, Seoul, South Korea

² Korea Institute of Atmospheric Prediction Systems, Seoul, South Korea

³ School of Natural Resources and Environmental Science, Kangwon National University, Chuncheon, South Korea

1 Introduction

Turbulent flow and pollutant dispersion in the convective boundary layer (CBL) have received much attention, particularly as regards atmospheric turbulence and air pollution, being affected by factors such as wind shear, surface heat flux, and surface roughness (e.g., Sykes and Henn 1989; Fedorovich 2004; Conzemius and Fedorovich 2006; Park and Baik 2014). To better understand turbulent flow and pollutant dispersion in the CBL, many field observational (Miao and Chen 2008; Zhang et al. 2016; Halios and Barlow 2018) and numerical modelling (Petersen et al. 1996; Khanna and Brasseur 1998; Petersen et al. 1999) studies have been made.

Turbulent flow in the CBL and the entrainment process at the top of the CBL have been numerically investigated using large-eddy simulation (LES) models (Mason 1989; Schmidt and Schumann 1989; Sykes and Henn 1989; Moeng and Sullivan 1994; Kim and Park 2003; Park and Baik 2014). Sykes and Henn (1989) examined turbulent flow in the CBL over a flat surface, and found that convective cells appear when the buoyancy effect is large and convective rolls appear when the effect of wind shear is large. It has been known that convective cells and rolls in the CBL play an important role in the transport of heat and momentum and affect the entrainment process at the CBL top (Moeng and Sullivan 1994; Khanna and Brasseur 1998; Kim and Park 2003). Kim et al. (2003) showed that wind shear changes the characteristics of the entrainment zone, in which large wind shear induces wavelike motions and increases the thickness of the entrainment zone and the magnitude of the heat flux. Sühring et al. (2014) investigated the effects of surface heat-flux heterogeneities on the entrainment process at and near the CBL top, and found that an entrainment maximum appears over the stronger or weaker heated regions due to the secondary circulations induced by the heat-flux heterogeneities. Park and Baik (2014) examined the CBL over an urban-like surface, represented by a block array, and over a flat surface. According to Park and Baik (2014), convective rolls are more likely to appear in the CBL over the urban-like surface than over the flat surface; in addition, analysis of the spectral density of vertical velocity reveals turbulent eddies produced by the block array. The flow speed in the CBL decreases due to the block array, resulting in an enhancement of wind shear in the entrainment zone, and increased turbulence intensity and magnitude of heat flux in the entrainment zone.

Not only turbulent flow but also the dispersion of passive and reactive pollutants in the CBL over a flat surface has been investigated using LES models (Schumann 1989; Henn and Sykes 1992; Krol et al. 2000; Vilà-Guerau de Arellano et al. 2004). According to Wyngaard and Brost (1984) and Moeng and Wyngaard (1984), passive scalar dispersion in the CBL is a superposition of bottom-up dispersion driven by the surface scalar flux and top-down dispersion driven by the entrainment scalar flux. Sorjan (2005, 2006) found that statistical moments of passive scalars in the CBL depend on parameters such as the Richardson number and convective velocity, with wind shear in the CBL affecting vertical profiles of statistical moments of passive scalar and scalar flux in the entrainment zone. Schumann (1989) studied the dispersion of two reacting fluid constituents in the CBL over a flat surface, finding that the reacting fluid constituent emitted from the surface is transported upward by updrafts related to convective cells or rolls. As a result, the reacting fluid constituent emitted from the surface exhibits high concentration in updraft regions. In contrast, the reacting fluid constituent included in air is transported downward by downdrafts related to convective cells or rolls and exhibits high concentration in downdraft regions. Vilà-Guerau de Arellano et al. (2004) studied the effects of turbulent structures in the CBL, such as convective cells and rolls, on reactive pollutant dispersion, and showed that turbulent structures in the CBL lead to

the segregation of reactive pollutants and reduce the chemical reaction rate. Krol et al. (2000) considered many chemically reactive species in the CBL. Turbulent flow in the CBL generates concentration fluctuations of chemically reactive species throughout the CBL, resulting in chemically unstable areas. When the emissions of chemically reactive species are spatially inhomogeneous, the effects of the segregation of chemically reactive species on the relevant chemical reactions increase and the chemical reaction rate decreases.

The aforementioned LES studies investigated reactive pollutant dispersion in the CBL over a flat surface. Buildings in urban areas modify flow and reactive pollutant dispersion significantly, and the effects of buildings on reactive pollutant dispersion have been investigated using idealized simulations (e.g., Baker et al. 2004; Chung and Liu 2012; Zhong et al. 2015). Zhong et al. (2016) reviewed reactive pollutant dispersion in street canyons. Park and Baik (2014) showed that buildings in urban areas modify the characteristics of the CBL. However, to the best of the authors' knowledge, there is no study that examines reactive pollutant dispersion in the CBL over an urban-like surface using a LES model despite its important implication to urban air pollution. The present study extends Park and Baik (2014) by taking account of reactive pollutants, and investigates turbulent flow and associated reactive pollutant dispersion in the CBL over an urban-like surface. In Sect. 2, descriptions of the LES model and simulation design are presented, and in Sect. 3, the LES model results are presented and discussed. In Sect. 4, a summary and conclusions are given.

2 LES Model and Simulation Design

To simulate turbulent flow and reactive pollutant dispersion in the CBL, we use version 4.0 of the parallelized LES model (PALM, Maronga et al. 2015), which is based on the filtered Navier–Stokes equations under the Boussinesq approximation. The filtered momentum, mass continuity, and thermodynamic energy equations are solved numerically, and to parametrize the subgrid-scale (SGS) fluxes, the 1.5-order Deardorff (1980) scheme and the SGS turbulence kinetic energy (TKE) equation are used. The governing equations are solved numerically using a finite difference scheme on the staggered Arakawa C-grid (Arakawa and Lamb 1977). The system of equations used in PALM is coupled with the transport equations for nitric oxide (NO), nitrogen dioxide (NO₂), and ozone (O₃) (Han et al. 2018), where the chemical reactions of NO, NO₂, and O₃ considered are as follows (Han et al. 2018),



Here, M represents a molecule that absorbs energy when O₃ is formed, and $h\nu$ represents a photon related to solar (shortwave) radiation. The photolysis rate of NO₂ in Eq. 1 (J_{NO_2}) and the rate constant in Eq. 3 (k_1) are calculated following Baik et al. (2007).

The simulation design is based on that of Park and Baik (2014), where the CBL over a flat surface without ambient flow (FNW case), the CBL over a flat surface with ambient flow (FW case), the CBL over a block array without ambient flow (BNW case), and the CBL over a block array with ambient flow (BW case) are simulated. Figure 1 shows the computational domain, and a block array is considered to imitate an urban-like surface (Park and Baik 2014). The array in the BNW and BW cases is composed of rectangular blocks, with the height and width of the blocks 80 m and 320 m, respectively. The separation of the blocks is 320 m,

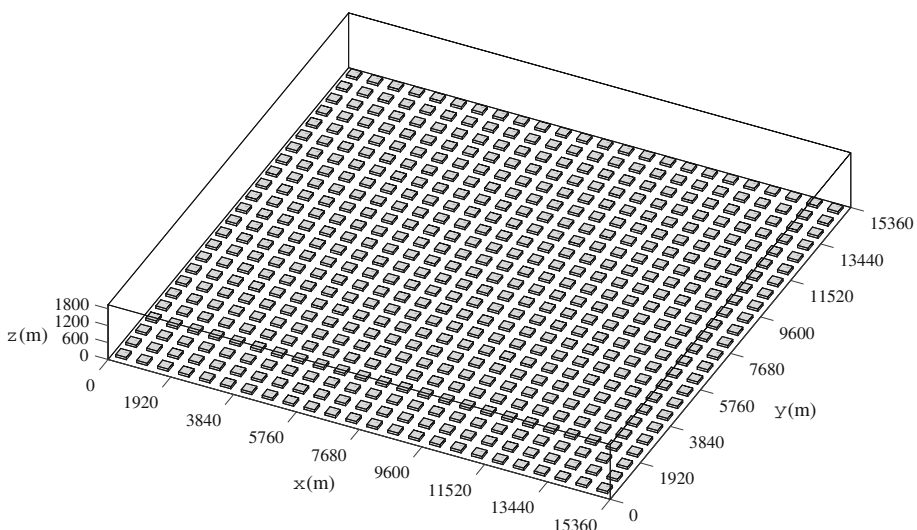


Fig. 1 Illustration of the computational domain and block array

and the aspect ratio of the urban-like canyon in the block array is 0.25; the plane area density of the block array is 0.25. The size of the computational domain is $15,360\text{ m} \times 15,360\text{ m} \times 1940\text{ m}$ in the x -, y -, and z -directions, with grid spacings in the x - and y -directions equal to 20 m. The grid spacing in the z -direction is 5 m up to $z = 80\text{ m}$ and increases algebraically by an expansion factor of 1.08 until the grid spacing in the z -direction becomes 10 m.

At the lateral boundaries, cyclic boundary conditions are applied for velocity, potential temperature, and reactive pollutants, and at the top boundary the zero-gradient boundary condition is applied for velocity. For potential temperature and reactive pollutants, vertical gradients of potential temperature and reactive pollutant concentration at the top boundary are kept constant, which are calculated from initial profiles of potential temperature and reactive pollutant concentration. At the grid points closest to the surface boundary (the ground and block surfaces), the Monin–Obukhov similarity with a roughness length of 0.1 m is employed in the momentum equation. Over an urban-like surface, the validity of the Monin–Obukhov similarity theory for momentum is not certain. Letzel et al. (2008) investigated the applicability of the Monin–Obukhov similarity theory for momentum to the simulation of turbulent flow near a cubical obstacle, and found that the LES results are well matched with the wind-tunnel data. Therefore, we speculate that the Monin–Obukhov similarity theory for momentum is applicable over the urban-like surface, though this issue needs a thorough investigation. In all cases, a surface heat flux with a magnitude of 0.1 K m s^{-1} , which is a moderate value in CBL studies using LES, is applied at the ground and at the tops of the blocks. The initial potential temperature is set to be 300 K from the ground to $z = 700\text{ m}$ and increases with a gradient of 0.015 K m^{-1} above $z = 700\text{ m}$. The initial potential temperature profile represents a well-developed CBL except for the surface layer, while the layer with constant potential temperature from the ground to $z = 700\text{ m}$ represents a mixed layer, and the layer with constant vertical gradient of potential temperature above $z = 700\text{ m}$ represents a capping inversion above the mixed layer. In many studies, similar initial potential temperature profiles are used to examine the CBL (e.g., Kim et al. 2003; Fedorovich 2004).

In the FW and BW cases, the initial ambient flow is in the positive x -direction with a speed of 10 m s^{-1} , which is large enough to show wind-shear effects in the CBL.

NO and NO_2 are emitted at the grid points closest to the ground. In the FNW and FW cases, the emission rates of NO and NO_2 are $2.5 \text{ ppb cell}^{-1} \text{ s}^{-1}$ and $0.25 \text{ ppb cell}^{-1} \text{ s}^{-1}$, respectively. In the BNW and BW cases, the emission rates of NO and NO_2 are $3.333 \text{ ppb cell}^{-1} \text{ s}^{-1}$ and $0.3333 \text{ ppb cell}^{-1} \text{ s}^{-1}$, respectively. The emission rates in the BNW and BW cases are larger than those in the FNW and FW cases, although the total emission amounts of NO and NO_2 in the model domain are the same in all cases because NO and NO_2 are not emitted where blocks are present. Dry deposition of reactive pollutants at the ground and block surfaces is not considered. In all cases, the initial background NO and NO_2 concentrations are 0 ppb and the initial background O_3 concentration is 50 ppb. The LES model is integrated for 2 h, and data in the last 600 s are used for analysis.

3 Results and Discussion

3.1 Turbulent Flow and Reactive Pollutant Dispersion

The vertical profiles of temporally- and horizontally-averaged vertical turbulent heat flux, potential temperature, velocity component in the x -direction, and TKE in the FNW, FW, BNW, and BW cases are shown in Fig. 2. Here, u and w represent the velocity components in the x - and z -directions, respectively, θ denotes the potential temperature, and e represents the TKE, with the overbar and angle bracket indicating temporal and horizontal averages, respectively. Prime denotes the perturbation, where the perturbation is defined as a deviation of the value of any variable from its horizontal average. For the temporal average, the last 600 s of simulation data are used. The CBL grows continuously, so that the CBL at the beginning and end of the averaging period can exhibit significantly different characteristics (e.g., potential temperature in the CBL and inversion height) if the average time period is too long. Therefore, we chose 600 s for the averaging period. In addition, our results show that the averaged vertical turbulent heat flux, potential temperature, velocity component in the x -direction, and TKE calculated using an average time period of 300 s (or 1200 s), are very similar to those calculated using 600 s. Therefore, the average time period of 600 s is acceptable to represent average characteristics of the CBL.

In all cases, the vertical turbulent heat flux decreases as the height increases in the mixed layer and shows a minimum in the entrainment zone (Fig. 2a). The vertical turbulent heat flux then increases with increasing height until it is close to zero. Following Park and Baik (2014), the inversion height is defined as the height at which the minimum value of the vertical turbulent heat flux appears, and the thickness of the entrainment zone is defined as the difference between the two heights where the vertical turbulent heat flux is close to zero. Table 1 lists the inversion height, thickness of the entrainment zone, vertical turbulent heat flux at the inversion height, and convective velocity in all cases. The thicknesses of the entrainment zones in the FW and BW cases are larger than those in the FNW and BNW cases; in particular, the BW case shows the largest thickness of the entrainment zone (300 m). Furthermore, the magnitude of the minimum vertical turbulent heat flux at the inversion height is largest in the BW case (0.017 K m s^{-1}). The thickness of the entrainment zone and the magnitude of the minimum vertical turbulent heat flux are related to the heat exchange in the entrainment zone (Park and Baik 2014). Therefore, it is concluded that the heat exchange in the entrainment zone in the BW case is larger than that in the FNW, FW, and BNW cases.

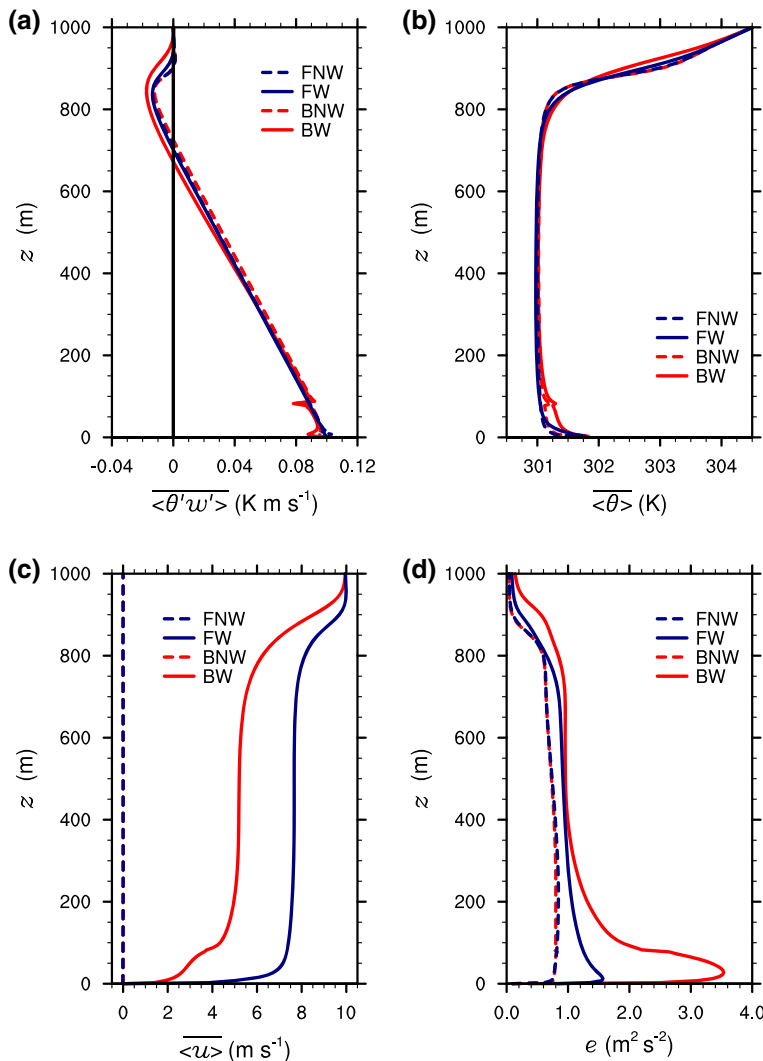


Fig. 2 Vertical profiles of temporally- and horizontally-averaged, **a** vertical turbulent heat flux, **b** potential temperature, **c** velocity component in the x -direction, and **d** TKE in the FNW, FW, BNW, and BW cases

In all cases, the surface layer, mixed layer, and entrainment zone appear clearly in the vertical profiles of the averaged potential temperature and velocity component in the x -direction (Fig. 2b, c). In the surface layer and mixed layer, the magnitude of $\langle u \rangle$ in the BW case is smaller than that in the FW case because of the presence of the block array, whereas the magnitudes of $\langle u \rangle$ in the free atmosphere are the same (10 m s^{-1}) in the FW and BW cases (Fig. 2c). As a result, the BW case displays greater wind shear in the entrainment zone than the FW case. According to Park and Baik (2014), wind shear in the entrainment zone enhances the heat exchange and increases turbulence intensity in the entrainment zone. Therefore, the largest magnitude of minimum vertical turbulent heat flux and the thickest

Table 1 Inversion height, thickness of the entrainment zone, vertical turbulent heat flux at the inversion height, and convective velocity in the FNW, FW, BNW, and BW cases

	FNW	FW	BNW	BW
Inversion height (m)	855	835	845	835
Thickness of entrainment zone (m)	180	220	170	300
$\overline{(\theta' w')}$ at inversion height (K m s^{-1})	-0.015	-0.012	-0.014	-0.017
Convective velocity (m s^{-1})	1.4	1.4	1.4	1.4

entrainment zone appear in the BW case (Fig. 2a); the TKE in the entrainment zone is also largest in the BW case (Fig. 2d).

The effects of the horizontal grid spacing on turbulent flow in the CBL were examined by performing two additional simulations. Simulation settings are the same as those for the BW case except for the computational domain size and the horizontal grid spacing. Considering the computing resources, the computational domain size of the additional simulations is reduced to 25% of the BW case, and the horizontal grid spacings of the simulations are 20 m and 10 m. The vertical profiles of vertical turbulent heat flux, potential temperature, velocity component in the x -direction, and TKE in the two additional simulations are similar (figures not shown). Therefore, the horizontal grid spacing of 20 m is acceptable in simulating flow in the CBL over the urban-like surface.

Figure 3 shows fields of vertical velocity, NO concentration, and O₃ concentration at $z = 400$ m (middle of the mixed layer) and $t = 7199$ s in the FNW, FW, and BW cases; the BNW case shows fields similar to the FNW case, thus the fields in the BNW case are omitted. The fields of NO₂ concentration are also omitted because they show spatial patterns similar to those of NO concentration. In the mixed layer, convective cells appear in the FNW case (Fig. 3a) and convective rolls appear in the FW and BW cases (Fig. 3b, c), with convective rolls in the BW case exhibiting more line-arranged structures than those in the FW case. The convective cells and rolls affect spatial distribution patterns of NO and O₃ in all cases. In updraft regions, NO concentration is high and O₃ concentration is low, mainly because air near the ground with high NO concentration and low O₃ concentration is transported by updrafts and the transported NO induces the O₃ decomposition. In downdraft regions, NO concentration is low and O₃ concentration is high due to the downward transport of air with low NO concentration and high O₃ concentration in the free atmosphere. Since air with high NO concentration and air with high O₃ concentration exist in updraft and downdraft regions, respectively, the two flow volumes are segregated from each other. This segregation of NO and O₃ interrupts O₃ decomposition (Schumann 1989).

According to Vilà-Guerau de Arellano et al. (2004), the segregation between reactive pollutants affects the chemical reaction rate when the time scale of chemical reactions is smaller than the time scale of turbulent motion. Below the inversion height, the time scale of turbulent motion calculated following Deardorff (1970) is ≈ 600 s. Following Vilà-Guerau de Arellano et al. (2004), the calculated time scales of NO and O₃ for Eq. 3 are ≈ 170 s and ≈ 30 s, respectively, and the calculated time scale of NO₂ for Eq. 1 is ≈ 120 s, so that time scales of NO, NO₂, and O₃ are smaller than the time scale of turbulent motion. Therefore, the chemical reactions occur before turbulent motion mixes air homogeneously, i.e., the segregation of the reactive pollutants affects the chemical reactions.

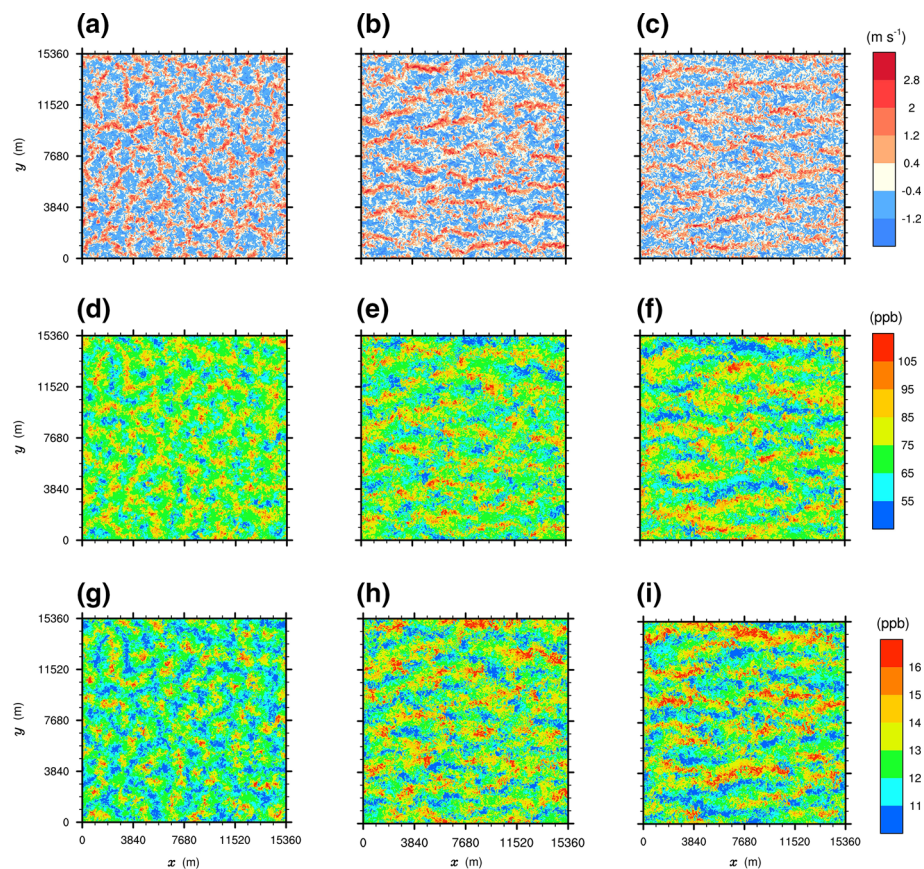


Fig. 3 Fields of vertical velocity in the, **a** FNW, **b** FW, and **c** BW cases, NO concentration in the **d** FNW, **e** FW, and **f** BW cases, and O₃ concentration in the **g** FNW, **h** FW, and **i** BW cases at $z = 400$ m and $t = 7199$ s

The correlation between the vertical velocity and reactive pollutant concentrations is calculated as the basis for quantitative analysis, with vertical velocity and NO and O₃ concentrations at $z = 400$ m and $t = 7199$ s used for the calculation. The correlation between the vertical velocity and NO concentration is 0.60 in all cases, indicating that high NO concentration generally appears in positive vertical velocity (updraft) regions and low NO concentration generally appears in negative vertical velocity (downdraft) regions. In contrast, the correlation between the vertical velocity and O₃ concentration is -0.55 in all cases, indicating that high O₃ concentration generally appears in negative vertical velocity regions and low O₃ concentration generally appears in positive vertical velocity regions. Therefore, the correlation analysis also reveals the segregation of NO and O₃.

In Fig. 3, convective cells and rolls appear clearly in the CBL, but other large-scale coherent structures are not evident in the CBL. To evaluate the effects of large-scale coherent structures on flow and reactive pollutant dispersion in the CBL, a spectral analysis was performed. The power spectral densities in the FW and BW cases show peaks due to the convective rolls, however, the power spectral densities in the FNW and BNW cases do not show peaks. Instead, the power spectral density at small wavenumbers in the FNW and BNW cases is larger than that in the FW and BW cases. It seems that energy of convective cells appears in the power

spectral density at small wavenumber. Therefore, we speculate that convective cells and rolls have the greatest effects on flow and reactive pollutant dispersion in the CBL and other large-scale coherent structures are less important in flow and reactive pollutant dispersion in the CBL. However, this issue needs further investigation.

Figure 4 shows vertical profiles of temporally- and horizontally-averaged NO, NO₂ and O₃ concentrations and O₃ production rate ($\langle J_{\text{NO}_2}[\text{NO}_2] - k_1[\text{O}_3][\text{NO}] \rangle$) in the FNW, FW, BNW, and BW cases. At $z = 2.5$ m, the averaged NO₂ and O₃ concentrations in all cases are approximately 60–70 ppb and 10 ppb, respectively. Although these concentration values appear in the idealized simulations, they also appear in observations of near-surface NO₂ and O₃ concentrations in urban areas (Mavroidis and Ilia 2012; Kwak et al. 2015). The averaged NO, NO₂, and O₃ concentrations do not change with height significantly in the mixed layer due to the convective mixing, while in the entrainment zone, the averaged NO, NO₂, and O₃ concentrations vary greatly with height (Fig. 4a–c). The magnitudes of the vertical gradients of the averaged NO, NO₂, and O₃ concentrations in the FW and BW cases are smaller than those in the FNW and BNW cases in the entrainment zone. This indicates that the reactive pollutant exchange in the entrainment zone is larger in the FW and BW cases than in the FNW and BNW cases. In the entrainment zone, the BW case shows the smallest magnitudes of the vertical gradients of the averaged NO, NO₂, and O₃ concentrations, implying that the reactive pollutant exchange in the entrainment zone is largest in the BW case, as for the heat exchange. It seems that the strengthened turbulent motion induced by the urban-like surface produces the large reactive pollutant exchange. In all cases, the magnitude of the O₃ production rate is large near the ground because of the high NO concentration near the ground (Fig. 4d). The BW case shows a negative peak at $z = 80$ m (the block height), and to investigate the negative peak at $z = 80$ m in the BW case, fields of velocity vector and NO concentration at $y = 8010$ m and $t = 6740$ s in the BW case are shown in Fig. 5. A large vortex formed between the blocks transports air with high NO concentration upward, and the transported NO decomposes O₃, thus the negative peak in the vertical profile of the O₃ production rate appears in the BW case. The O₃ production rate in the mixed layer is nearly zero in all cases, implying that the mixed layer is close to chemical equilibrium. The profile of the O₃ production rate displays a negative peak in the entrainment zone in all cases because the reactive pollutant exchange in the entrainment zone induces O₃ decomposition.

To investigate the effects of turbulent flow on the chemical reactions, the averaged O₃ production rate is separated as follows,

$$\langle J_{\text{NO}_2}[\text{NO}_2] - k_1[\text{O}_3][\text{NO}] \rangle = \overline{\langle J_{\text{NO}_2} \rangle \langle [\text{NO}_2] \rangle} - \overline{\langle k_1 \rangle \langle [\text{O}_3] \rangle \langle [\text{NO}] \rangle} - \overline{\langle k_1 \rangle \langle [\text{O}_3]' [\text{NO}]' \rangle}. \quad (4)$$

On the right-hand side of Eq. 4, the components of the averaged O₃ production rate related to the perturbations of the photolysis rate of NO₂ (J'_{NO_2}) and the rate constant (k'_1) are ignored. This is because the components of the averaged O₃ production rate related to J'_{NO_2} and k'_1 are much smaller than the averaged O₃ production rate in the mixed layer and entrainment zone. Below $z = 940$ m, the sum of the components of the averaged O₃ production rate related to J'_{NO_2} and k'_1 is less than 15% of the averaged O₃ production rate. The first and second terms on the right-hand side of Eq. 4 are related to the horizontally-averaged concentrations and the third term on the right-hand side of Eq. 4 is related to the concentration perturbations. Hereafter, the sum of the first and second terms of Eq. 4 ($\langle J_{\text{NO}_2} \rangle \langle [\text{NO}_2] \rangle - \overline{\langle k_1 \rangle \langle [\text{O}_3] \rangle \langle [\text{NO}] \rangle}$) and the third term of Eq. 4

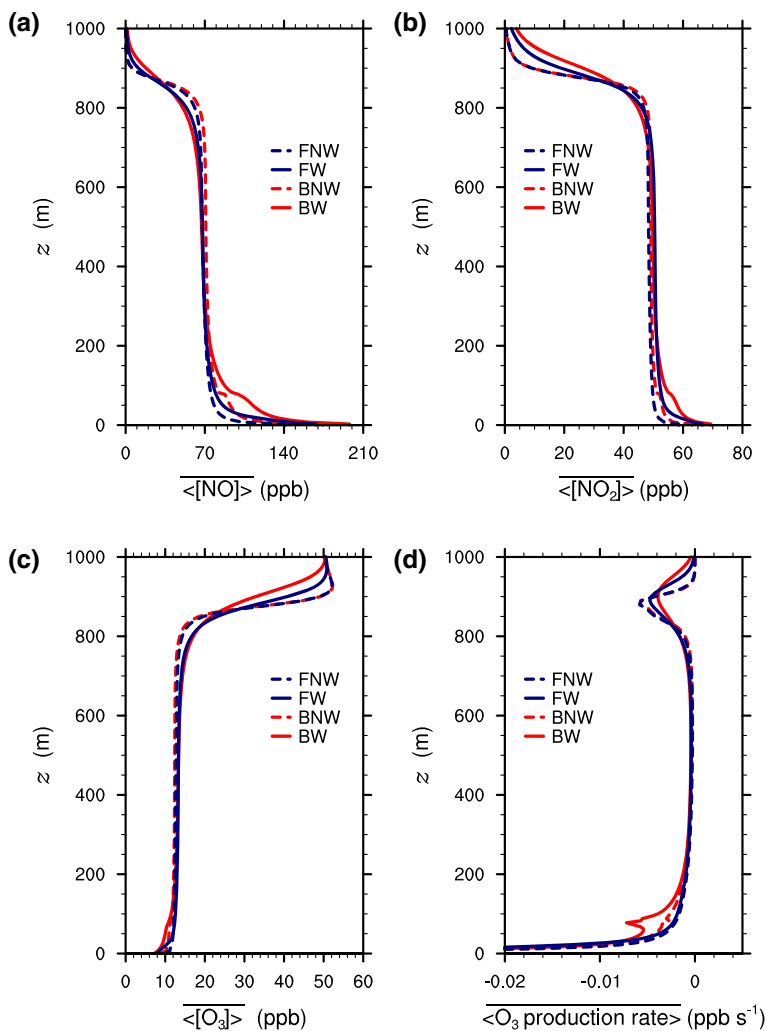


Fig. 4 Vertical profiles of temporally- and horizontally-averaged, **a** NO concentration, **b** NO₂ concentration, **c** O₃ concentration, and **d** O₃ production rate in the FNW, FW, BNW, and BW cases

$\left(-\langle k_1 \rangle \langle [O_3]'[NO]' \rangle \right)$ are referred to as the mean and turbulent components of the O₃ production rate, respectively.

Figure 6 shows vertical profiles of the mean and turbulent components of the O₃ production rate in the FNW, FW, BNW, and BW cases. In all cases, the mean component of the O₃ production rate is generally negative due to the high NO concentration near the ground (Fig. 6a). The vertical profile of the mean component displays a negative peak in the entrainment zone due to the reactive pollutant exchange, with the magnitudes of the peaks in the FW and BW cases smaller than those in the FNW and BNW cases. This is because the large reactive pollutant exchange due to the wind shear in the FW and BW cases decreases the magnitudes of the vertical gradients of the averaged NO, NO₂, and O₃ concentrations in the entrainment zone. Since the urban-like surface induces greater wind shear in the entrainment

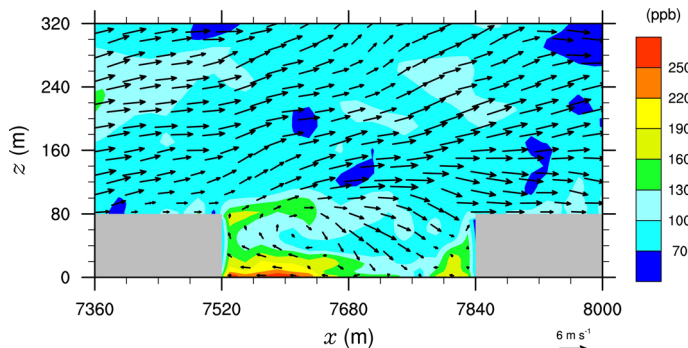


Fig. 5 Fields of the velocity vector and NO concentration at $y = 8010$ m and $t = 6740$ s in the BW case

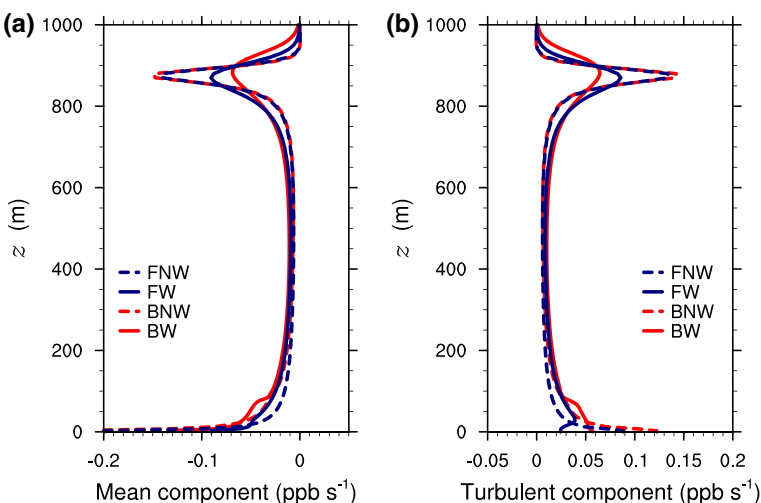


Fig. 6 Vertical profiles of the, **a** mean component and **b** turbulent component of the O_3 production rate in the FNW, FW, BNW, and BW cases

zone, the BW case displays the peak with the smallest magnitude. The width of the peak is related to the thickness of the entrainment zone, i.e., the thickness of the layer in which the chemical reactions occur actively is related to the thickness of the entrainment zone. Therefore, the width of the peak is larger in the FW and BW cases than in the FNW and BNW cases and the largest width of the peak appears in the BW case. NO and O_3 are segregated spatially, thus the signs of NO and O_3 concentration perturbations are generally opposite. As a result, the turbulent component of the O_3 production rate is generally positive in all cases (Fig. 6b), noting that the turbulent component represents the effects of the segregation on the chemical reactions. The positive value of the turbulent component means that the O_3 decomposition in the CBL is reduced due to the segregation. The vertical profiles of the turbulent component in all cases have positive peaks in the entrainment zone, indicating that the reduction of the O_3 decomposition due to the segregation is greatest in the entrainment zone. In the FW and BW cases, the magnitude of the peak is smaller compared to the FNW and BNW cases, and the smallest magnitude of the peak appears in the BW case. It seems that the turbulent motion strengthened by the wind shear in the entrainment zone mixes the

reactive pollutants and weakens the effects of the segregation on the chemical reactions. In all cases, the magnitude of the mean component is slightly larger than that of the turbulent component below the inversion height. The differences between the magnitudes of the mean and turbulent components are less than 20% below the inversion height, except near the ground. These results indicate that the segregation of NO and O₃ has important effects on the chemical reactions below the inversion height.

To examine the effects of block height, a simulation with doubled block height (160 m, double-height case) was performed. In the double-height case, the grid spacing in the *z*-direction is 5 m up to *z* = 160 m and increases algebraically by an expansion factor of 1.08 until the grid spacing in the *z*-direction becomes 10 m. Other simulation settings are identical to the BW case. In the CBL, the magnitude of $\langle u \rangle$ in the double-height case is smaller than that in the BW case because of the greater block height. Since the magnitudes of $\langle u \rangle$ in the free atmosphere are almost the same in the BW and double-height cases, the double-height case displays greater wind shear in the entrainment zone than the BW case. Due to the enhanced wind shear in the entrainment zone, the double-height case shows the greater turbulence intensity and heat and reactive pollutant exchange in the entrainment zone.

Since the NO and NO₂ emission rates and background O₃ concentration can modify reactive pollutant dispersion and chemical reactions in the CBL, the effects of the NO and NO₂ emission rates and background O₃ concentration need to be examined. For this, two additional simulations were performed. One simulation has doubled NO and NO₂ emission rates (6.666 ppb cell⁻¹ s⁻¹ for NO and 0.6666 ppb cell⁻¹ s⁻¹ for NO₂, double-NO_x case), and the other simulation has doubled O₃ background concentration (100 ppb, double-O₃ case). Other simulation settings are identical to the BW case. The averaged NO and NO₂ concentrations in the CBL are larger in the double-NO_x case than in the BW case. Compared to the BW case, the higher averaged NO concentration causes smaller averaged O₃ concentration in the CBL. The averaged O₃ concentration in the CBL in the double-O₃ case is larger than that in the BW case, and compared to the BW case, the higher O₃ concentration causes smaller averaged NO concentration and larger averaged NO₂ concentration in the CBL. Below the inversion height (*z* = 835 m), the averaged NO₂ concentration in the double-O₃ case is larger than that in the double-NO_x case, implying that the chemical reactions are more important than the emission rate for increasing NO₂ concentration below the inversion height. In the double-NO_x case, the magnitude of the averaged O₃ production rate near the ground is smaller than that in the BW case due to the decreased O₃ concentration and increased NO₂ concentration. In contrast, the magnitude of the averaged O₃ production rate near the CBL top in the double-NO_x case is larger than that in the BW case due to the increased NO concentration. In the double-O₃ case, the magnitude of the averaged O₃ production rate near the ground is larger than that in the BW case due to the increased O₃ concentration.

The effects of heterogeneous emission on reactive pollutant dispersion are also examined, using a simulation in which the emission rate of NO is 13.333 ppb cell⁻¹ s⁻¹ in the centre region ($5760 \text{ m} \leq x \leq 9600 \text{ m}$ and $5760 \text{ m} \leq y \leq 9600 \text{ m}$) of the computational domain and 2.667 ppb cell⁻¹ s⁻¹ in the rest of the computational domain. The emission rate of NO₂ is one-tenth of that of NO. The total emission amounts of NO and NO₂ in the computational domain are the same as those in the BW case. Other simulation settings are identical to the BW case. In the heterogeneous emission case, high NO and low O₃ concentrations appear in the range from *y* = 5760 to 9600 m due to the heterogeneous emission. The heterogeneous emission changes the spatial distribution of the reactive pollutants, which induces the greater reduction of the O₃ decomposition due to the segregation.

3.2 Reactive Pollutant Exchange and Chemical Reactions in the Entrainment Zone

Figure 7 shows fields of vertical velocity, NO concentration perturbation, and vertical turbulent NO flux ($[NO]'w'$) at $z = 850$ m (the inversion height) and $t = 7199$ s in the FNW, FW, and BW cases. At $z = 850$ m, strong updrafts and downdrafts tend to appear above updraft regions of the convective cells and rolls (Fig. 7a–c). Also, the positive NO concentration perturbation at $z = 850$ m generally appear above updraft regions of the convective cells and rolls, due to the upward transport of NO (Fig. 7d–f). As a result, the magnitude of $[NO]'w'$ at $z = 850$ m is large above updraft regions of the convective cells and rolls (Fig. 7g–i). At $z = 850$ m, NO_2 and O_3 also show characteristics similar to NO, except that the sign of the O_3 concentration perturbation (vertical turbulent O_3 flux) is opposite to that of NO concentration perturbation (vertical turbulent NO flux).

Figure 8 shows fields of the O_3 production rate at $z = 850$ m and $t = 7199$ s in the FNW, FW, and BW cases. In centres of strong updraft regions, air with high NO concentration transported by strong updrafts is not mixed well with air with high O_3 concentration at $z = 850$ m. Therefore, the magnitude of the O_3 production rate is generally small in centres of

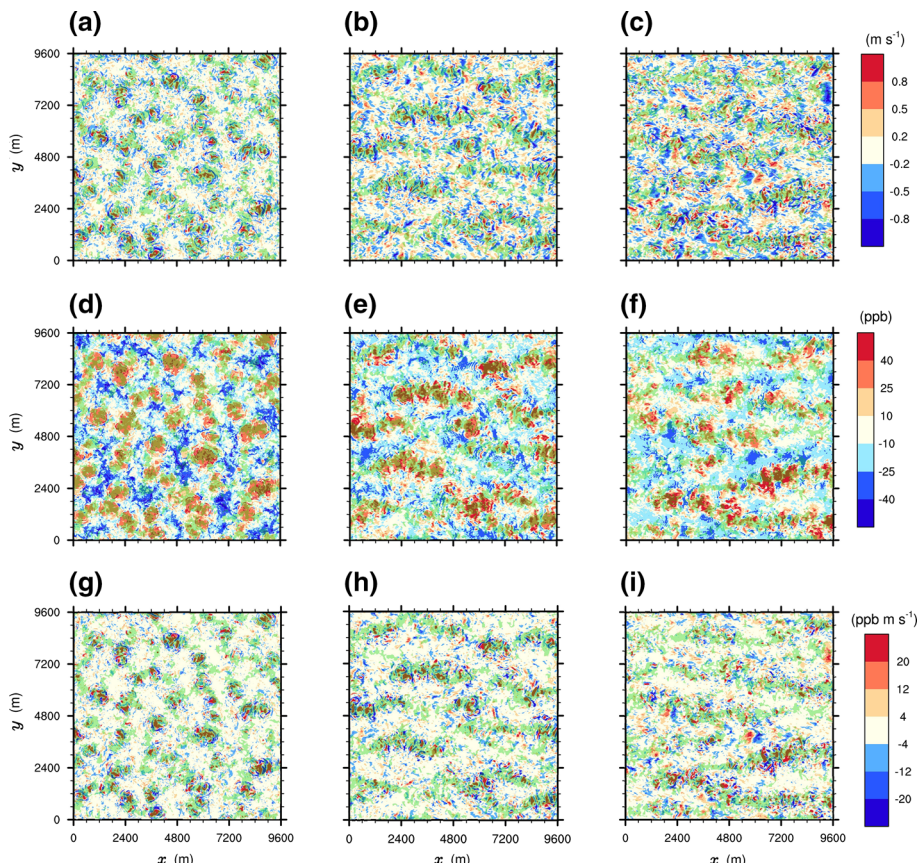


Fig. 7 Fields of vertical velocity in the, **a** FNW, **b** FW, and **c** BW cases, NO concentration perturbation in the **d** FNW, **e** FW, and **f** BW cases, and vertical turbulent NO flux in the **g** FNW, **h** FW, and **i** BW cases at $z = 850$ m and $t = 7199$ s. The areas where the vertical velocity $> 0.2 \text{ m s}^{-1}$ at $z = 400$ m are indicated in green

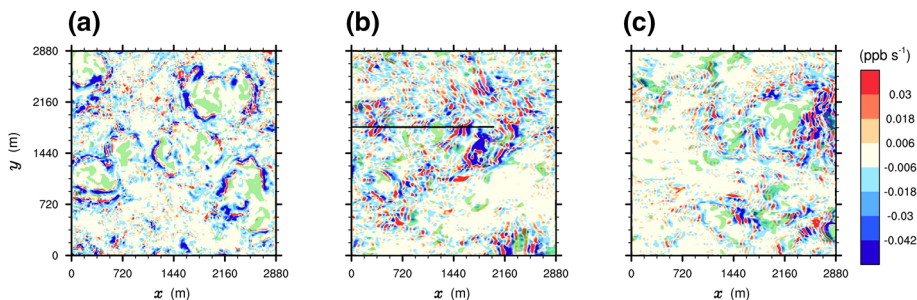


Fig. 8 Fields of the O_3 production rate at $z = 850$ m and $t = 7199$ s in the, **a** FNW, **b** FW, and **c** BW cases. The areas where the vertical velocity $> 0.1 \text{ m s}^{-1}$ at $z = 850$ m are indicated in green. The black line in Fig. 8b represents the location of graphs in Fig. 9

strong updraft regions (Fig. 8a–c). Around strong updraft regions, air with high NO and NO_2 concentrations transported by strong updrafts is mixed with air with high O_3 concentration at $z = 850$ m. As a result, the magnitude of the O_3 production rate is generally large around strong updrafts regions.

The O_3 production and decomposition occur alternatively, especially in the FW and BW cases (Fig. 8b, c). To examine the alternating O_3 production and decomposition, the variations of NO, NO_2 , and O_3 concentration perturbations and the magnitudes of the positive ($J_{NO_2}[NO_2]$) and negative ($-k_1[O_3][NO]$) terms of the O_3 production rate at $z = 850$ m, $y = 1810$ m, and $t = 7199$ s in the FW case are analyzed (Fig. 9). At $z = 850$ m, the averaged NO and NO_2 concentrations are similar (47 ppb for NO and 43 ppb for NO_2). However, the magnitude of the NO concentration variation is larger than that of the NO_2 concentration variation (Fig. 9a) because the magnitudes of the NO and NO_2 concentration variations are related to the averaged NO and NO_2 concentrations in the mixed layer. Since the magnitude of the NO concentration variation is larger than that of NO_2 , NO concentration is generally larger (smaller) than NO_2 concentration when NO and NO_2 concentrations are at local maxima (minima) (Fig. 9a). Therefore, the magnitude of the negative term of the O_3 production rate ($-k_1[O_3][NO]$) tends to be larger (smaller) than the magnitude of the positive term of the O_3 production rate ($J_{NO_2}[NO_2]$) when NO and NO_2 concentrations are at local maxima (minima) (Fig. 9b). Since local maxima and minima of NO and NO_2 concentrations appear alternatively, the alternating O_3 production and decomposition occur in the entrainment zone. In the FNW and BNW cases, the averaged NO concentration is higher than the averaged NO_2 concentration, and the turbulence intensity is smaller than that in the FW and BW cases. As a result, NO_2 concentration higher than NO concentration appears rarely, and areas where O_3 production occurs also appear rarely, compared to the FW and BW cases.

3.3 Effects of Chemical Reactions

Additional simulations without the chemical reactions for NO, NO_2 , and O_3 are performed to examine the effects of the chemical reactions on NO, NO_2 , and O_3 concentrations. Figure 10 shows fields of differences in O_3 concentration between the simulations with and without the chemical reactions at $z = 850$ m and $t = 7199$ s in the FNW and BW cases. The difference in O_3 concentration is negative in almost all areas in Fig. 10, i.e., O_3 concentration decreases due to the chemical reactions. In the FNW and BW cases, the magnitude of the concentration difference is large in updraft regions at $z = 400$ m because updrafts transport air with low

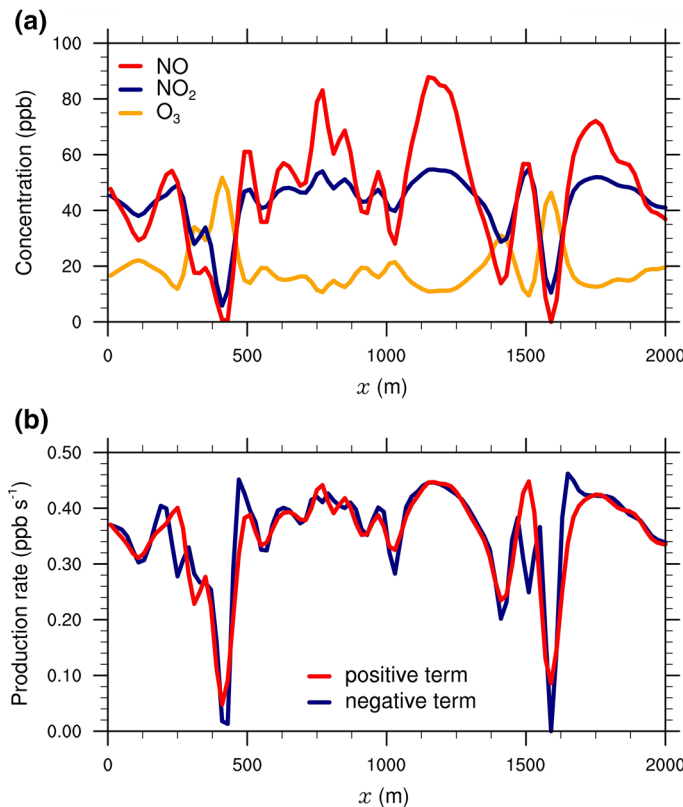


Fig. 9 Variations of **a** NO, NO₂, and O₃ concentrations and **b** the magnitudes of the positive ($J_{\text{NO}_2}[\text{NO}_2]$) and negative ($-k_1[\text{O}_3][\text{NO}]$) terms of the O₃ production rate at $z = 850$ m, $y = 1810$ m, and $t = 7199$ s in the FW case

O₃ concentration upward due to the chemical reactions. This distribution pattern of the O₃ concentration difference appears in the mixed layer and entrainment zone in all four cases.

To compare the changes of NO, NO₂, and O₃ concentrations due to the chemical reactions quantitatively, the *CE* (chemical effect), defined by Han et al. (2018), is calculated from

$$CE = 100 \times \left(\frac{\overline{c_{\text{chem}}}}{\overline{c_{\text{nochem}}}} - 1 \right), \quad (5)$$

where c_{chem} denotes the reactive pollutant concentration in the simulation with the chemical reactions and c_{nochem} denotes the reactive pollutant concentration in the simulation without the chemical reactions. The vertical *CE* profiles of NO, NO₂, and O₃ in the FNW, FW, BNW, and BW cases are presented in Fig. 11. Below the inversion height, the chemical reactions increase the averaged NO₂ concentration by 360% in all cases (Fig. 11b). The chemical reactions decrease the averaged NO and O₃ concentrations by 35% and 74% below the inversion height, respectively (Fig. 11a, c). Below the inversion height, the mean and turbulent components of the O₃ production rate have opposite signs because of the spatial segregation of NO and O₃ (Fig. 6), and so the O₃ decomposition rate in the CBL is decreased significantly, i.e., NO and O₃ are less consumed and NO₂ is less produced. As a result, the *CE* values of NO and O₃ increase and the *CE* value of NO₂ decreases. When the reactive

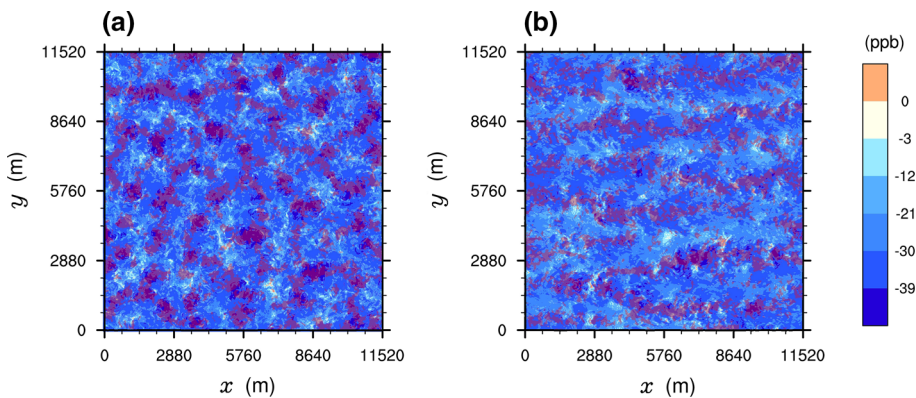


Fig. 10 Fields of differences in O_3 concentration between the simulations with and without the chemical reactions at $z = 850$ m and $t = 7199$ s in the, **a** FNW, and **b** BW cases. The areas where the vertical velocity $> 0.2 \text{ m s}^{-1}$ at $z = 400$ m are indicated in red

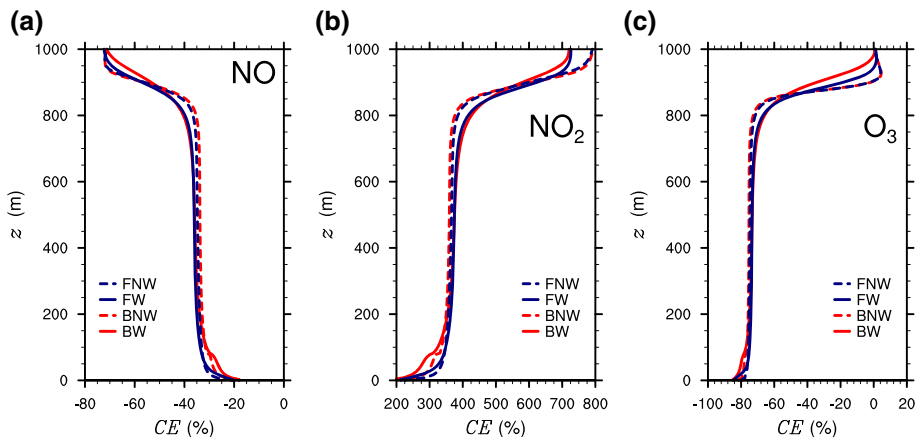


Fig. 11 Vertical CE profiles of, **a** NO concentration, **b** NO_2 concentration, and **c** O_3 concentration in the FNW, FW, BNW, and BW cases

pollutant exchange is large because of the wind shear in the entrainment zone, the magnitudes of the vertical gradients of the averaged reactive pollutants become small. Consequently, the magnitudes of the vertical CE gradients in the FW and BW cases are smaller than those in the FNW and BNW cases, and the BW case shows the smallest magnitudes of the vertical CE gradients due to the enhanced wind shear in the entrainment zone.

The different NO and NO_2 emission rates and background O_3 concentration change the CE values of NO , NO_2 , and O_3 . In the double- NO_x case, the CE magnitudes of NO and NO_2 are smaller than those in the BW case because NO and NO_2 concentrations increase significantly, but the changes of NO and NO_2 concentrations due to the chemical reactions do not increase much. In contrast, the CE magnitude of O_3 in the double- NO_x case is larger than that in the BW case because the increased NO concentration induces active O_3 decomposition. In the double- O_3 case, the CE magnitudes of NO and NO_2 below the inversion height are larger than those in the BW case because the higher background O_3 concentration increases the changes of NO and NO_2 concentrations due to the chemical reactions. In contrast, the CE

magnitude of O₃ in the double-O₃ case is smaller than that in the BW case due to the increase of O₃ concentration.

4 Summary and Conclusions

We investigated turbulent flow and associated reactive pollutant dispersion in the convective boundary layer (CBL) over a block array representing an urban-like surface and a flat surface using a LES model that includes the transport equations for NO, NO₂, and O₃. The CBL over a flat surface with and without ambient flow (FW and FNW cases, respectively) and the CBL over a block array with and without ambient flow (BW and BNW cases, respectively) were simulated and compared.

Compared to the FNW and BNW cases, the FW and BW cases show the larger turbulence intensity and heat exchange due to the wind shear in the entrainment zone. In the entrainment zone, the urban-like surface enhances the wind shear, thus the BW case shows the largest turbulence intensity and heat exchange. In the CBL, NO and O₃ are spatially segregated from each other, and NO and O₃ concentrations are relatively high in updraft and downdraft regions, respectively. In the entrainment zone, the BW case shows the smallest magnitude of the vertical gradients of the averaged NO, NO₂, and O₃ concentrations, indicating that the reactive pollutant exchange in the entrainment zone is largest in the BW case. It seems that the wind shear enhanced by the urban-like surface in the entrainment zone induces larger reactive pollutant exchange in the entrainment zone. All cases show negative peaks in the O₃ production rate in the entrainment zone because the reactive pollutant exchange in the entrainment zone induces vigorous O₃ decomposition. The turbulent components of the O₃ production rate represent the effects of segregation on the chemical reactions. The turbulent component shows positive peaks in the entrainment zone, and the magnitude of the positive peaks is smallest in the BW case. This result shows that the reduction of the O₃ decomposition due to the segregation in the entrainment zone is smallest in the BW case. It seems that the effects of segregation on the chemical reactions are reduced due to the strengthened turbulent motions in the BW case.

Strong updrafts and downdrafts in the entrainment zone generally appear above updraft regions in the mixed layer. The magnitude of the O₃ production rate is large around strong updraft regions due to the mixing of air from the mixed layer and air in the entrainment zone. In the FW and BW cases, the O₃ production and decomposition appear alternatively in the entrainment zone because the O₃ production and decomposition tend to occur when NO and NO₂ concentrations decrease and increase, respectively. Below the inversion height, the chemical reactions increase the averaged NO₂ concentration in all cases by 360%, whereas the chemical reactions decrease the averaged NO and O₃ concentrations in all cases by 35% and 74%, respectively.

In this study, dispersion of the reactive pollutants and their chemical reactions in the CBL over a block array and a flat surface were examined with an aim of providing insight into reactive pollutant dispersion in the daytime urban boundary layer. Different block sizes and arrays can induce changes in turbulent flow and reactive pollutant dispersion therein, deserving investigation. Also, the present study considers only NO, NO₂, and O₃ and their photochemical reactions, thus further studies using LES with complex chemical processes are encouraged.

Acknowledgements The authors are grateful to three anonymous reviewers for providing valuable comments on this work. This work was supported by Basic Science Research Program through the National Research Foundation of Korea (NRF) funded by the Ministry of Science and ICT (No. 2016R1A2B2013549).

References

- Arakawa A, Lamb VR (1977) Computational design of the basic dynamical processes of the UCLA general circulation model. *Methods Comput Phys* 17:173–265
- Baik JJ, Kang YS, Kim JJ (2007) Modeling reactive pollutant dispersion in an urban street canyon. *Atmos Environ* 41:934–949
- Baker J, Walker HL, Cai X (2004) A study of the dispersion and transport of reactive pollutants in and above street canyons—a large eddy simulation. *Atmos Environ* 38:6883–6892
- Chung TNH, Liu CH (2012) Large-eddy simulation of reactive pollutant dispersion for the spatial instability of photostationary state over idealised 2D urban street canyons. *Int J Environ Pollut* 50:2–6
- Conzemius RJ, Fedorovich E (2006) Dynamics of sheared convective boundary layer entrainment. Part I: methodological background and large-eddy simulations. *J Atmos Sci* 63:1151–1178
- Deardorff JW (1970) Convective velocity and temperature scales for the unstable planetary boundary layer and Rayleigh convection. *J Atmos Sci* 27:1211–1213
- Deardorff JW (1980) Stratocumulus-capped mixed layers derived from a three-dimensional model. *Boundary-Layer Meteorol* 18:495–527
- Fedorovich E (2004) Dispersion of passive tracer in the atmospheric convective boundary layer with wind shears: a review of laboratory and numerical model studies. *Meteorol Atmos Phys* 87:3–21
- Halios CH, Barlow JF (2018) Observations of the morning development of the urban boundary layer over London, UK, taken during the ACTUAL project. *Boundary-Layer Meteorol* 166:395–422
- Han BS, Baik JJ, Kwak KH, Park SB (2018) Large-eddy simulation of reactive pollutant exchange in and above a street canyon. *Atmos Environ* 187:381–389
- Henn DS, Sykes RI (1992) Large-eddy simulation of dispersion in the convective boundary layer. *Atmos Environ* 26:3145–3159
- Khanna S, Brasseur JG (1998) Three-dimensional buoyancy- and shear-induced local structure of the atmospheric boundary layer. *J Atmos Sci* 55:710–743
- Kim SW, Park SU (2003) Coherent structures near the surface in a strongly sheared convective boundary layer generated by large-eddy simulation. *Boundary-Layer Meteorol* 106:35–60
- Kim SW, Park SU, Moeng CH (2003) Entrainment processes in the convective boundary layer with varying wind shear. *Boundary-Layer Meteorol* 108:221–245
- Krol MC, Molemaker MJ, Vilà-Guerau de Arellano J (2000) Effects of turbulence and heterogeneous emissions on photochemically active species in the convective boundary layer. *J Geophys Res Atmos* 105:6871–6884
- Kwak KH, Baik JJ, Ryu YH, Lee SH (2015) Urban air quality simulation in a high-rise building area using a CFD model coupled with mesoscale meteorological and chemistry-transport models. *Atmos Environ* 100:167–177
- Letzel MO, Krane M, Raasch S (2008) High resolution urban large-eddy simulation studies from street canyon to neighbourhood scale. *Atmos Environ* 42:8770–8784
- Maronga B, Gryschka M, Heinze R, Hoffmann F, Kanani-Sühring F, Keck M, Ketelsen K, Letzel MO, Sühring M, Raasch S (2015) The Parallelized Large-Eddy Simulation Model (PALM) version 4.0 for atmospheric and oceanic flows: model formulation, recent developments, and future perspectives. *Geosci Model Dev* 8:2515–2551
- Mason PJ (1989) Large-eddy simulation of the convective atmospheric boundary layer. *J Atmos Sci* 46:1492–1516
- Mavroidis I, Ilia M (2012) Trends of NO_x, NO₂ and O₃ concentrations at three different types of air quality monitoring stations in Athens, Greece. *Atmos Environ* 63:135–147
- Miao S, Chen F (2008) Formation of horizontal convective rolls in urban areas. *Atmos Res* 89:298–304
- Moeng CH, Sullivan PP (1994) A comparison of shear- and buoyancy-driven planetary boundary layer flows. *J Atmos Sci* 51:999–1022
- Moeng CH, Wyngaard J (1984) Statistics of conservative scalars in the convective boundary layer. *J Atmos Sci* 41:3161–3169
- Park SB, Baik JJ (2014) Large-eddy simulations of convective boundary layers over flat and urbanlike surfaces. *J Atmos Sci* 71:1880–1892

- Petersen AC, Beets C, Krol MC (1996) Parametrization of segregation effects due to convective boundary-layer mixing in atmospheric chemistry models. *Phys Chem Earth* 21:445–450
- Petersen AC, Beets C, van Dop H, Duynkerke PG, Siebesma AP (1999) Mass-flux characteristics of reactive scalars in the convective boundary layer. *J Atmos Sci* 56:37–56
- Schmidt H, Schumann U (1989) Coherent structure of the convective boundary layer derived from large-eddy simulations. *J Fluid Mech* 200:511–562
- Schumann U (1989) Large-eddy simulation of turbulent diffusion with chemical reactions in the convective boundary layer. *Atmos Environ* 23:1713–1727
- Sorjan Z (2005) Statistics of scalar fields in the atmospheric boundary layer based on large-eddy simulations. Part I: free convection. *Boundary-Layer Meteorol* 116:467–486
- Sorjan Z (2006) Statistics of scalar fields in the atmospheric boundary layer based on large-eddy simulations. Part II: forced convection. *Boundary-Layer Meteorol* 119:57–79
- Sühring M, Maronga B, Heribert F, Raasch S (2014) On the effect of surface heat-flux heterogeneities on the mixed-layer-top entrainment. *Boundary-Layer Meteorol* 151:531–556
- Sykes RI, Henn DS (1989) Large-eddy simulation of turbulent sheared convection. *J Atmos Sci* 46:1106–1118
- Vilà-Guerau de Arellano J, Dosio A, Vinuesa JF, Holtslag AAM, Galmarini S (2004) The dispersion of chemically reactive species in the atmospheric boundary layer. *Meteorol Atmos Phys* 87:23–38
- Wyngaard JC, Brost R (1984) Top-down and bottom-up diffusion of a scalar in the convective boundary layer. *J Atmos Sci* 41:102–112
- Zhang Y, Wang Y, Chen G, Smeltzer C, Crawford J, Olson J, Szykman J, Weinheimer AJ, Knapp DJ, Montzka DD, Wisthaler A, Mikoviny T, Fried A, Diskin G (2016) Large vertical gradient of reactive nitrogen oxides in the boundary layer: modeling analysis of DISCOVER-AQ 2011 observations. *J Geophys Res Atmos* 121:1922–1934
- Zhong J, Cai XM, Bloss WJ (2015) Modelling segregation effects of heterogeneous emissions on ozone levels in idealised urban street canyons: using photochemical box models. *Environ Pollut* 188:132–143
- Zhong J, Cai XM, Bloss WJ (2016) Coupling dynamics and chemistry in the air pollution modelling of street canyons: a review. *Environ Pollut* 214:690–704

Publisher's Note Springer Nature remains neutral with regard to jurisdictional claims in published maps and institutional affiliations